

Shaped, on-demand microwave single-photon generator

P. Forn-Díaz,^{1,2,3} C. W. Warren,¹ C. W. S. Chang,¹ A. M. Vadiraj,¹ and C. M. Wilson¹

¹*Institute for Quantum Computing and Department of Electrical and Computer Engineering, University of Waterloo, 200 University Avenue West, Waterloo, N2L 3G1, Canada*

²*Escola Tècnica Superior d'Enginyeria Industrial de Barcelona, Universitat Politècnica de Catalunya, Barcelona, 08034, Spain*

³*Barcelona Supercomputing Center (BSC), C/ Jordi Girona 29, 08034, Barcelona. Spain*

(Dated: July 28, 2022)

We demonstrate the full functionality of a circuit that generates single microwave photons on-demand, with a wavepacket that can be modulated with a near-arbitrary shape. We achieve such a high tunability by coupling a superconducting qubit near the end of a semi-infinite transmission line. A DC-SQUID shunts the line to ground and is employed to modify the spatial dependence of the electromagnetic mode structure in the transmission line. This allows us to couple and decouple the qubit from the line, shaping its emission rate on fast-time scales. Our decoupling scheme is applicable to all types of superconducting qubits and other solid state systems and can be generalized to multiple qubits as well as to resonators.

I. INTRODUCTION

Quantum networks are a promising paradigm both for quantum communication and quantum computation. A quantum network consists of a set of quantum processing nodes between which quantum information is communicated using quantum channels [1]. Individual photons are promising information carriers between quantum nodes given the robustness of their quantum states and the possibility to travel long distances, both in the optical [2] as well as the microwave frequency domain [3]. For quantum networks and other purposes, single-photon generators are therefore an enabling resource. A list of desirable characteristics for a single-photon source include high efficiency, on-demand (deterministic) operation, and low timing jitter in the emission. In order to achieve maximum state transfer efficiency between quantum nodes, it is also desirable to controllably shape the photon wave packet, such that it matches the absorption profile of the receiving node [4]. Single-photon sources have other applications beyond quantum communication, such as preparing nonclassical states of harmonic oscillators which can be used in certain quantum error correcting protocols [5].

Superconducting qubits are ideal candidates to behave as tunable single-photon sources in the microwave domain. There have already been implementations of single-photon sources made from qubits coupled to resonators [6–9], including circuits with tunable waveforms [10–12]. While shown to be useful for specific applications such as Hong-Ou-Mandel interferometry [13, 14], the usage of a cavity in these implementations intrinsically limits the source to a single frequency. Working instead with qubits directly coupled to propagating modes of radiation enables the engineering of tunable, highly efficient single-photon sources [15]. In recent years, experiments have demonstrated basic operations of a single qubit interacting with propagating modes such as resonance fluorescence [16], a single-photon router [17], quantum-state filtering [18] and photon-mediated interactions [19, 20].

Recent experiments using transmission lines have demonstrated a frequency-tunable single-photon source with a flux qubit capacitively coupled to two semi-infinite lines [21] and the correlated emission of photons at two different frequencies using a transmon qubit [22]. Both experiments used fixed qubit-line couplings. Despite all the progress, no experiment to date has demonstrated a qubit-line interaction that can be controllably switched off, an important advantage in efficiently transferring quantum states between remote nodes of a quantum network [1]. Recent theoretical proposals have suggested the use of a DC-SQUID as an adjustable impedance to modify the spatial profile of vacuum fluctuations along a semi-infinite transmission line, [23, 24], thereby controlling the photon emission rate of the qubit. The basic principle of this tunable-coupling scheme was demonstrated in an earlier experiment [25], but only with static tuning. Besides the relevant applicability as a tunable single-photon source, a system with a tunable interaction to a continuum of modes would allow fundamental studies of light-matter interaction including generalizations of the Lamb shift [26].

Here, we implement a superconducting circuit that generates single, shaped microwave photons on-demand, with low timing jitter, and with high efficiency. Our device consists of a DC-SQUID operating as a tunable shunt in a semi-infinite transmission line, together with a capacitively coupled transmon qubit [27] positioned a specific distance from the end of the line. The relative simplicity of the device, compared to its high performance, is enabled by the versatility and novelty of our tunable-coupling scheme.

II. PRINCIPLE OF OPERATION

Our circuit consists of a semi-infinite transmission line, the *source* line, with a DC-SQUID acting as an inductive shunt embedded at its end (see Fig. 1(a)). The impedance presented by the SQUID can be tuned with

the application of an external magnetic flux Φ_{SQ} . In this configuration, the SQUID effectively behaves as an electrical mirror with an adjustable position, which is complementary to a recent experiment where a qubit was instead effectively moved by tuning its frequency [25]. We galvanically connect a high-bandwidth transmission line, the *current* line, to the SQUID loop to enable fast tuning of Φ_{SQ} . Using galvanic coupling maximizes the amount of dissipation produced by the applied current pulses. A superconducting transmon qubit [27] is capacitively coupled at a specific distance from the end of the source line. A separate on-chip microwave line, the *excitation* line, is weakly coupled to the qubit enabling direct driving of the qubit even when it is decoupled from the source line. The designed qubit frequency is such that the distance L between the qubit and the end of the source line corresponds approximately to a half wavelength, $L = \lambda/2 = \pi v/\omega_{01}$, where v is the speed of light in the line and ω_{01} is the frequency corresponding to the $|0\rangle \rightarrow |1\rangle$ qubit transition. The shunted end of the line imposes a boundary condition on the spectral density of modes, which is then position-dependent according to [25]

$$S(\omega) = 2\hbar\omega \cos^2[\theta(L) + \phi(\Phi_{\text{SQ}})]. \quad (1)$$

The phase $\theta(L)$ contains the geometric position dependence. For a qubit with frequency $\omega_{01} = 2\pi v/\lambda_{01}$ this phase has the value $4\pi L/\lambda_{01} + \pi$, with the π contribution accounting for reflection from the end of a shorted transmission line. The flux-tunable phase $\phi(\Phi_{\text{SQ}})$ is the contribution from the finite SQUID inductance, which is often described as a change of the effective electrical length of the line. As a consequence of changing the electrical length, the position of the field nodes and antinodes at a given frequency along the source line can be controlled, modifying the interaction strength with the qubit, as shown in Fig. 1(a). The maximum dynamic range of the coupling is obtained for an electrical length between the qubit and the end of the line corresponding to $\lambda_{01}/2$ (modulo λ_{01}). Ideally, at $\Phi_{\text{SQ}} = 0$ the SQUID impedance would be zero and we would have a voltage node at the qubit position. At $\Phi_{\text{SQ}}/\Phi_0 = 0.5$, with Φ_0 the flux quantum, the SQUID would ideally have an infinite impedance, changing the electrical length of the line by $\lambda/4$, thereby placing a voltage antinode at the qubit. In practice, the tuning range of the SQUID is finite and we cannot change the electrical length by the full $\lambda/4$.

To understand how modifying the vacuum mode structure affects the qubit-line coupling, we recall that any quantum emitter coupled to a continuum of modes will experience energy decay due to vacuum fluctuations of the continuum. Following from Fermi's Golden Rule, the emission rate, Γ_1 , is proportional to the spectral density of modes at the emitter frequency, $\Gamma_1 \sim S(\omega_{01})$. It was shown [25] that for a transmon qubit in front of a mirror the precise relation is $\Gamma_1 = Z_0(e/\hbar)^2(C_s/C_\Sigma)^2 S(\omega_{01})\sqrt{E_J/2E_C}$. Here, Z_0 is

the impedance of the line, C_s is the qubit-line capacitance, $C_\Sigma = C_s + C_J$ is the total capacitance including the qubit self-capacitance C_J , E_J is the qubit Josephson energy, and E_C is the qubit charging energy. With $S(\omega_{01})$ in the source line given by Eq. (1), we see that the emission rate into the line can be tuned by adjusting the electrical length of the line by, e.g., changing $\phi(\Phi_{\text{SQ}})$. In this work, we use this effect to continuously tune Γ_1 on short time scales by adjusting Φ_{SQ} .

In order to build an on-demand photon generator, we first apply a magnetic flux through the SQUID that sets $S(\omega_{01}) = 0$ exactly at the qubit position (red curve in Fig. 1(a)), suppressing qubit emission into the line. The qubit can then be prepared in an arbitrary state by exciting it using the excitation line, which is always coupled. Using the fast current line, a current pulse of arbitrary shape modifies $\Phi_{\text{SQ}}(t)$ in real time which translates into a shift of the position of vacuum field nodes. The qubit is then coupled to the vacuum fluctuations (blue curve in Fig. 1(a)) and spontaneously emits a photon which contains the information of the qubit state in its I/Q quadratures [7]. As the qubit-line coupling can be controlled in real-time by the SQUID current pulse, the emitted photons can be shaped arbitrarily.

In our experiment, we use a single-junction, fixed-frequency transmon to keep λ_{01} fixed. We could extend our circuit's capabilities to allow tuning of the frequency of the emitted photons by using a standard tunable-frequency transmon without modifying any of the protocols presented in this work.

III. DEVICE DESCRIPTION

A micrograph of a device similar to the one measured is shown in Fig. 1(b). The transmon qubit capacitively couples to the source line over a length of 300 μm with an estimated capacitance of $C_s \approx 28.3$ fF (see Fig. 1(c)). The distance from the qubit to the end of the line is $L = 9.59$ mm. The excitation line is weakly coupled to one of the qubit capacitor plates with $C_e \approx 0.9$ fF. The current line galvanically coupled to the SQUID loop is symmetrically split (see Fig. 1(d)).

Qubit spectroscopy can be performed directly by measuring the reflection of a probing field (see Fig. 1(b)). Alternatively, the qubit spectrum can be measured in transmission by using the excitation line as input port. Using both methods, we measure a qubit frequency of $\omega_{01}/2\pi = 3.690$ GHz with anharmonicity $\alpha/2\pi = -141.7$ MHz, yielding a total qubit capacitance of $C_\Sigma = 136$ fF, $E_J/E_C = 91$, $E_J/h = 12.9$ GHz and a qubit critical current of $I_C = 26$ nA. Based on images of similar devices to the one measured, we estimate a SQUID critical current of $I_{\text{SQ}} = 130$ nA, with the SQUID junctions nominally identical. With this value of critical current, the SQUID inductance follows closely the expected $L_{\text{SQ}}^{-1} \sim |\cos(\pi\Phi_{\text{SQ}}/\Phi_0)|$ since its geometric inductance can be mostly neglected.

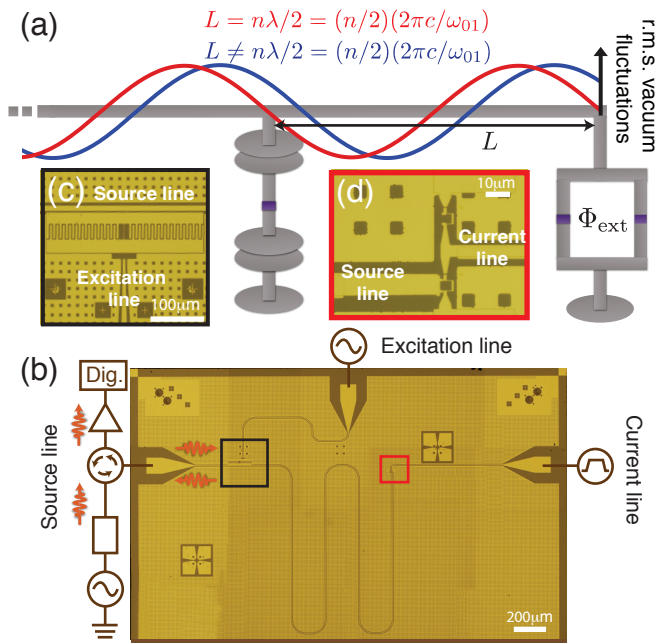


FIG. 1. (a) Cartoon of the device operating principle. A DC-SQUID shunts the line to ground and a flux threading it controls the profile of the r.m.s. amplitude of the vacuum fluctuations. We plot a single mode for clarity, but the effect is broadband. A qubit positioned at an integer of half-wavelengths ($L = n\lambda/2$) at its resonance frequency, depicted in red, will be effectively decoupled from the line. For other conditions with $L \neq n\lambda/2$, depicted in blue, the qubit will be coupled to a variable degree. (b) Optical image of a device similar to the one used in the experiment and circuit schematic. The output from the source line is amplified at different stages and digitized at room temperature. (c) Optical image of the single-junction transmon qubit capacitively coupled to the transmission line. The excitation line has a weak, fixed coupling to the qubit, allowing its state to be controlled irrespective of the coupling strength to the source line. (d) Optical image of the SQUID shunting the source line to ground. The current line connecting from the left is used to tune the SQUID flux Φ_{SQ} in real time.

We spectroscopically characterize the system by measuring the reflection of a coherent signal off the circuit with the reflection coefficient $r \equiv \langle V_r \rangle / \langle V_{\text{in}} \rangle$, where $\langle V_r \rangle$ and $\langle V_{\text{in}} \rangle$ are the phase-sensitive averages of the reflected and incident voltages, respectively. In Ref. [25], it was shown that for a weak probe,

$$r = -1 + \frac{\Gamma_1}{\Gamma_2 + i\delta\omega}, \quad (2)$$

with $\Gamma_2 = \Gamma_1/2 + \Gamma_\phi$ being the total decoherence rate and Γ_ϕ the pure dephasing rate. $\delta\omega = \omega_{01} - \omega_d$ is the drive detuning from the qubit frequency ω_{01} . Γ_1 is the emission rate of the qubit into the transmission line and therefore quantifies the qubit-line coupling strength.

Figure 2 shows qubit decay rates extracted from spectroscopy measured in reflection, as a function of Φ_{SQ} . When Φ_{SQ} is an integer multiple of Φ_0 , the qubit ex-

hibits a maximum decay rate $\Gamma_1/2\pi = 1.9$ MHz. Within a flux period, there are two points where the decay rate is observed to approximately vanish, $\Phi_{\text{SQ}}^{(1)}/\Phi_0 = 0.39$ and $\Phi_{\text{SQ}}^{(2)}/\Phi_0 = 0.61$. At these flux values, the qubit signal is lost, indicating a clear decoupling from the source line. At these points the driving field does not excite the qubit and the signal is fully reflected. The modulation of Γ_1 is a signature of the tunability of the qubit-line interaction. The observed maximum and minimum of Γ_1 allow us to

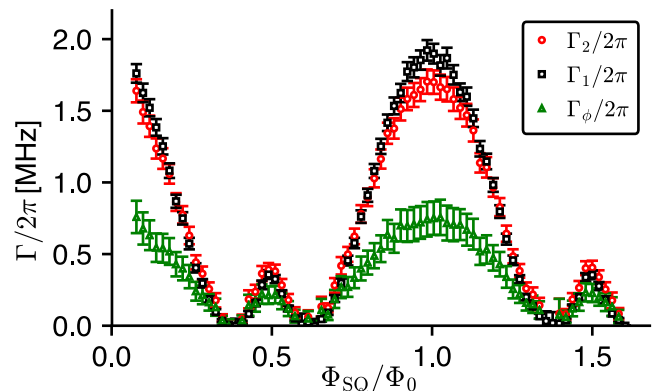


FIG. 2. Extracted qubit decay rates. The qubit emission rate into the source line, Γ_1 , (black squares) and the total decoherence rate, Γ_2 , (red circles) are obtained from Eq. (2). The pure dephasing rate Γ_ϕ is calculated as $\Gamma_\phi = \Gamma_2 - \Gamma_1/2$. All three rates tune with flux, showing a clear modulation of the qubit-source line coupling strength.

place a bound on the ON/OFF ratio of the decoupling mechanism at ≈ 190 . The qubit frequency is also modulated with the external flux by a small amount (not shown), even though this is a single-junction transmon qubit. This frequency shift will be the study of future work [28].

As explained in Sec. II, the maximum tuning range of the device is ideally a displacement of the standing wave profile by $\lambda_{01}/4$. Besides the limitations already mentioned, another important condition must be met: a voltage node or antinode needs to be located at the qubit position at zero flux $\Phi_{\text{SQ}} = 0$. In other words, the length between qubit and the end of the line L needs to match an integer n of half wavelengths, $L = n\lambda_{01}/2$. This is difficult to achieve exactly given the normal spread in device fabrication parameters. Given the observed recovery of the emission rate at $\Phi_{\text{SQ}}/\Phi_0 = 0.5$, we estimate that with the present device the standing wave is displaced by $\lambda/5.13$, limiting in this case the ON/OFF ratio and the rate of photon emission (the dynamic range). This can be circumvented with a frequency-tunable qubit or a more accurate design of qubit wavelength λ_{01} .

The pure dephasing rate Γ_ϕ clearly modulates along with the qubit-line coupling until saturating at a value of $\Gamma_\phi/2\pi \approx 0.7$ MHz in the range of flux $\Phi_{\text{SQ}}/\Phi_0 = 0.9-1.1$. We do not currently have a clear explanation for this dependence.

IV. DRIVEN QUBIT DYNAMICS

We can also see the tunability of the qubit-source line coupling in the real-time dynamics of the qubit when a coherent microwave control pulse is applied. Our detected signals correspond to the quadratures of the field emitted by the qubit $\langle I(t) \rangle, \langle Q(t) \rangle$, where the expectation value is evaluated for the qubit state at the time of emission. Each individual time trace is typically averaged 10^6 times. As already demonstrated in previous work using a transmon qubit coupled to a resonator [6, 7], the qubit coherence is mapped to the state of the emitted photon. Following the standard result from input-output theory [6], given the existing direct relationship between the qubit emission operator $\langle \sigma^- \rangle$ and the quadratures of the emitted field $\langle (a \pm a^\dagger) \rangle$ [29], a maximum of the recorded signal corresponds to the qubit in a superposition state on the equatorial plane of the Bloch sphere, such as $|\pm\rangle = (|0\rangle \pm |1\rangle)/\sqrt{2}$.

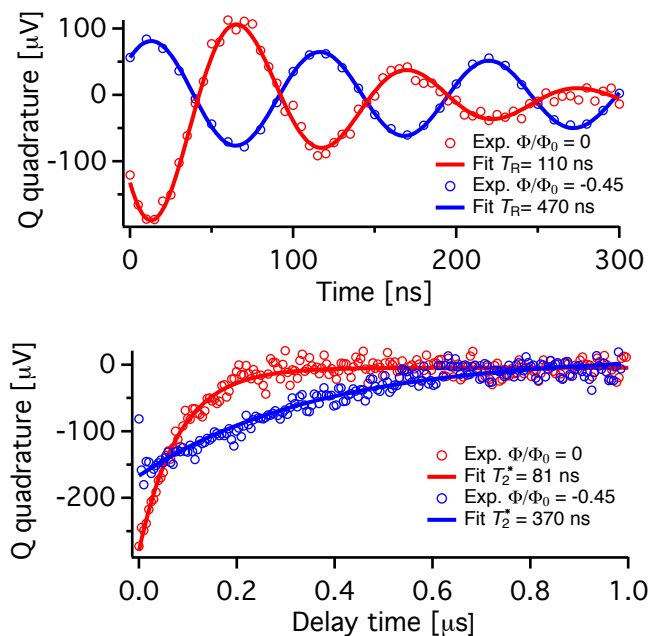


FIG. 3. Qubit dynamics at two operating flux bias points with higher (red) and lower (blue) qubit-source line coupling rate. (a) Rabi oscillations. The Rabi decay times, T_R , differ by a factor 4.3. (b) Free induction decay of the qubit state after a $\pi/2$ pulse. The decay rate is enhanced 4.6 times between the two bias points. The enhanced coupling of the qubit into the line is further evidenced by a larger qubit signal for the shortest-lived traces, both for the free decay as well as the Rabi oscillations.

Fig. 3(a) shows Rabi oscillations of the qubit biased at two different bias points with significantly different coupling to the source line, while Fig. 3(b) shows free decay of the qubit after a $\pi/2$ pulse. The Rabi oscillations are obtained by integrating free decay traces such as those in Fig. 3(b) at different Rabi pulse lengths. The integrated value is then normalized to the number of points.

In all traces in Fig. 3, the signal is maximized by digitally rotating it into the Q quadrature. The red data points in Figs. 3(a)-(b) correspond to $\Phi_{SQ}/\Phi_0 = 0$, which means the phase drop $\phi(0)$ in Eq. (1) is minimal. The observed Rabi oscillations at $\Phi_{SQ} = 0$ in Fig. 3(a) decay with a characteristic time of $T_R = 110$ ns. The emitted qubit signal is maximum after a $\pi/2$ pulse since we are recording the qubit quadratures and therefore the qubit coherence $\langle \sigma^- \rangle$. The qubit free decay in Fig. 3(b) at $\Phi_{SQ} = 0$ is $T_2^* = 81$ ns when prepared in a superposition state. This decay time corresponds to a decay rate of $\Gamma_2/2\pi = 1.96$ MHz, which is consistent with the spectroscopic value of Γ_2 in Fig. 2. The blue data points in Figs. 3(a)-(b) correspond to $\Phi_{SQ}/\Phi_0 = -0.45$. The Rabi oscillations observed in Fig. 3(a) are clearly longer lived compared to those at $\Phi_{SQ}/\Phi_0 = 0$, indicating a lower qubit-source line coupling. The decay of the Rabi oscillations at this bias point is $T_R = 470$ ns, about four times longer than the decay at $\Phi_{SQ}/\Phi_0 = 0$. The free decay of the qubit signal in Fig. 3(b) is measured to be $T_2^* = 370$ ns. Both in Figs. 3(a) and 3(b), the amplitude of the qubit signal at $\Phi_{SQ}/\Phi_0 = -0.45$ is lower compared to the signal at $\Phi_{SQ}/\Phi_0 = 0$. This is another clear indication of the modulation of the qubit-source line coupling strength.

To demonstrate the nonclassical nature of the emitted radiation, we recorded the second moment of the emitted field which corresponds to the emitted power $\langle P \rangle \equiv \langle (I^2 + Q^2) \rangle$. Fig. 4 shows the evolution of $\langle I \rangle$ and $\langle P \rangle$ during Rabi oscillations. Two traces are shown with the first (black) and second (red) moments of the driven qubit biased at $\Phi_{SQ}/\Phi_0 = -0.45$, where the decay time is long. The signal was averaged over 2.5×10^7 repetitions as $\langle P \rangle$ is rather noisy. The clear oscillatory pattern recovered after all those averages is a manifestation of the coherence of the radiation emitted by the qubit. The phase of the power oscillation is clearly offset by approximately $\pi/2$ with respect to the quadrature amplitude oscillation, as is expected for a single-photon emitter such as our transmon qubit. For a coherent state, one would expect $\langle I_c^2 \rangle = \langle I_c \rangle^2$, therefore power and amplitude should oscillate in-phase. In contrast, for the qubit state $\cos(\theta/2)|0\rangle + \sin(\theta/2)|1\rangle$ we get [29] $\langle I_q \rangle \sim \langle \sigma^- \rangle \sim \sin \theta$ and $\langle P_q \rangle \sim 1 + \langle \sigma_z \rangle \sim 1 - \cos \theta$, consistent with the observations in Fig. 4. This is strong evidence that the source of photons is nonclassical [6].

V. TRIGGERED PHOTON GENERATION

As mentioned in the introduction, triggered photon emission is important for transferring quantum states in a quantum network with high efficiency.

In order to demonstrate triggered photon emission with our circuit, we add a current pulse through the current line (see Fig. 1(b)). The current pulse tunes $\phi(\Phi_{SQ})$ in Eq. (1), allowing fast tuning of the qubit-source line coupling strength. The external field is first set to zero,

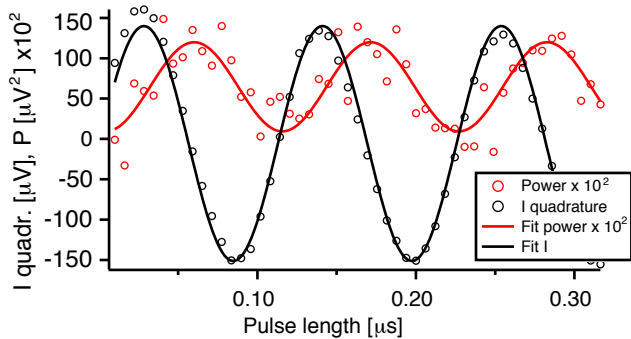


FIG. 4. Power and quadrature oscillations of emitted radiation from the driven qubit. Black circles represent the measured I quadrature amplitude, while red circles correspond to the second moment of the emission, the emitted power $\langle P \rangle = \langle (I^2 + Q^2) \rangle$. The solid curves are sinusoidal fits to the data. The two curves are offset by $(0.58 \pm 0.08)\pi$, which rules out a coherent state and provides strong evidence of single-photon emission.

$\Phi_{SQ} = 0$, where the qubit is strongly coupled to the line, as shown in Fig. 2. Figure 5 shows a schematic of the pulse scheme. A square current pulse is applied to bring the qubit to the decoupling bias point. Then, a pulse in the excitation line energizes the source. (For these experiments, we use a $\pi/2$ pulse to maximize the emitted quadrature signal, although a π pulse would be used to produce a pure single photon.) The excitation can now be stored for a maximum of the intrinsic relaxation time of the qubit $T_{1,\max}$. At a desired time, the current pulse returns the qubit to a strongly coupled point, where the excitation is emitted with a “jitter” corresponding to the emission time of the qubit T_1 at that bias point.

Figure 5 shows the observed emission pattern following the pulse scheme just described. Each trace corresponds to a different storage time. The traces are vertically displaced for clarity. At a delay time of $0.5 \mu\text{s}$, a peak is always detected which corresponds to the excitation pulse leaking into the source line. The first trace shows a decaying tail of 65 ns immediately after the driven pulse. This corresponds to the emission of this particular device when it is excited at the bias point with maximum qubit coupling to the line. The emission pattern is similar to previous observations of single-photon sources with fixed coupling [6, 21, 22]. In the rest of the traces, the qubit excitation is stored for a controlled amount of time. The emission of the qubit can be still be detected with delay times up to $2 \mu\text{s}$ for this particular device, demonstrating triggered emission of photons on-demand.

The ratio of the storage time and the jitter time is a figure of merit for an “on-demand” source. First, it is useful to be able to separate in time the excitation pulse and the single-photon emission, e.g., because the excitation pulse can blind detectors. Second, in applications where photon timing is important, the emission time of the photon T_1 represents a jitter (uncertainty) in the ef-

fective emission time. Minimizing this at fixed coupling, however, would limit the preparation fidelity, as the qubit will partially decay during the excitation pulse. The minimization of jitter time in combination with a long storage time is therefore an important advantage of our photon generator over other implementations. The decay time obtained from Fig. 5 corresponds to the decoherence time T_2^* since the qubit is excited in a superposition state. It corresponds to a jitter of $T_1 = 46 \text{ ns}$, using the dephasing rate obtained in Fig. 2.

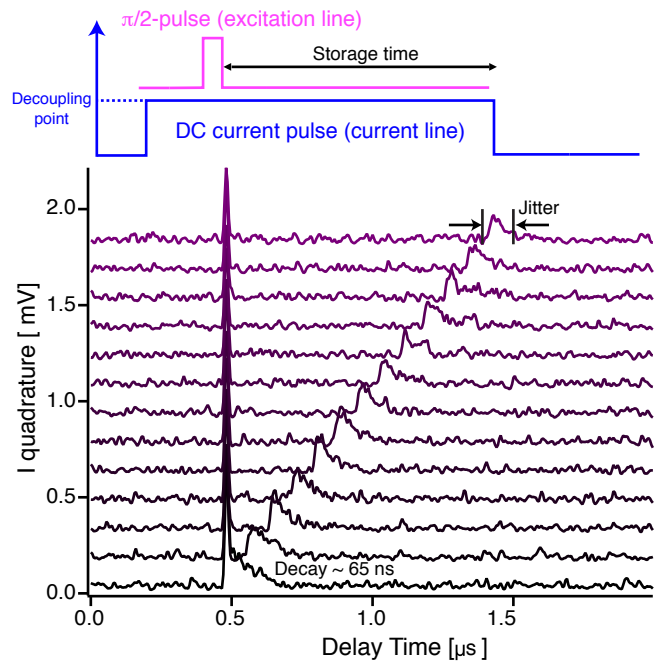


FIG. 5. On-demand single-photon generation. The pulse sequence begins by bringing the qubit to the decoupling point by pulsing current through the SQUID and then exciting the qubit with a $\pi/2$ -pulse. The qubit emission is triggered by ending the current pulse through the SQUID, bringing the qubit back to a strongly coupled point. The peak registered near $0.5 \mu\text{s}$ is the excitation pulse partially leaking into the measurement chain circuit.

In future work, the scheme is to be combined with a frequency tunable qubit. This will allow the color of the emitted photons to be changed without compromising the emission efficiency, as is the case in other proposed single-photon source schemes based on qubits in cavities.

VI. SHAPED PHOTON GENERATION

The qubit emission can be further controlled in real time by sending shaped current pulses through the current line. In this way, the qubit emission rate $\Gamma_1(\Phi_{SQ}(t))$ can be adjusted nearly arbitrarily. Recent theoretical work [23, 30] studied how the controlled emission then produces a known photon wavepacket with amplitude $\xi(t)$. Figure 6 displays several examples of measured

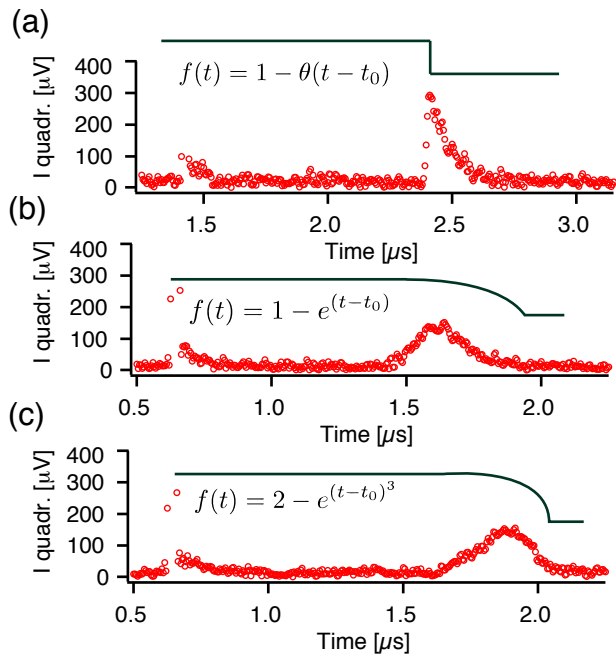


FIG. 6. Shaped photon generation. (a)-(c) show the emission of the source given different current modulation $f(t)$, sketched with the black traces above the data. (a) Emitted qubit voltage with a sharp falling edge. The qubit emission is clearly exponential. (b) Same as (a) but using a falling exponential edge. The qubit emission looks nearly symmetric. (c) The falling edge of the SQUID current pulse is an inverted cubic exponential. The qubit emission in this case approaches the time-reverse of the emission in (a). The signal recorded $1 \mu\text{s}$ prior to the qubit emission corresponds to the excitation pulse.

shaped-photon emission. Panel (a) shows the exponentially decaying signal from a sharp-edged DC-SQUID current pulse, which is the same profile observed in Fig. 5. Panel (b) displays a nearly symmetric signal achieved by modulating the trailing edge of the DC pulse by an inverted exponential. Panel (c) shows the emission from an inverted cubic exponential which resembles a time-reversed version from the original exponential pulse in panel (a). Our electronics were limited in this experiment, but, in principle, an arbitrary wavepacket could be produced with fast-enough pulse shaping. As mentioned in the introduction, the ability to produce shaped pulses controllably is very relevant for good absorption of photon pulses by distant nodes of a quantum network.

VII. PHOTON GENERATION EFFICIENCY

Finally, we can use our ability to control the photon emission to directly measure the intrinsic qubit coherence times which are necessary to calculate the photon generation efficiency. Adapting from a technique developed at NEC [29], we first apply a π pulse to the qubit at the decoupling point which excites it in the state $|1\rangle$. The qubit

excitation decays with its intrinsic rate $\Gamma_{1,i} = 1/T_{1,i}$ due to the microscopic environment in what we refer to as nonradiative decay. This decay may include emission into other transmission lines, such as the excitation line, even though we estimate that channel loss to be negligible. Our observations cannot rule out that the qubit at the decoupling point has a remaining but small coupling to the source line, limiting the intrinsic relaxation time $T_{1,i}$. After a varying delay τ , a $\pi/2$ pulse is applied to the qubit to rotate it onto the σ_x/σ_y plane, followed by a current pulse which brings the qubit to a strongly emitting bias point. The $\pi/2$ pulse converts the remaining qubit population into a detectable field quadrature amplitude, as was shown in Fig. 3. The integrated signal shown in Fig. 7(a) for a varying delay leads us directly to an intrinsic relaxation time $T_{1,i} = 2.86 \mu\text{s}$, which is a typical value for a transmon qubit with a nonoptimized geometry.

Similarly, we can obtain the intrinsic dephasing time of the qubit $T_{2,i}^*$ by biasing it at the decoupling point and exciting it directly with a $\pi/2$ pulse, as shown in Fig. 7(b). By controlling the delay time between the $\pi/2$ pulse and the end of the current pulse, we directly monitor the leftover qubit coherence. The integrated signal leads us to $T_{2,i}^* = 1.33 \mu\text{s}$, also in agreement with other experiments using planar transmon devices in resonators [6, 7, 9, 10]. The obtained coherence times are compatible with a pure intrinsic qubit dephasing time of $T_{\phi,i} = 2.49 \mu\text{s}$.

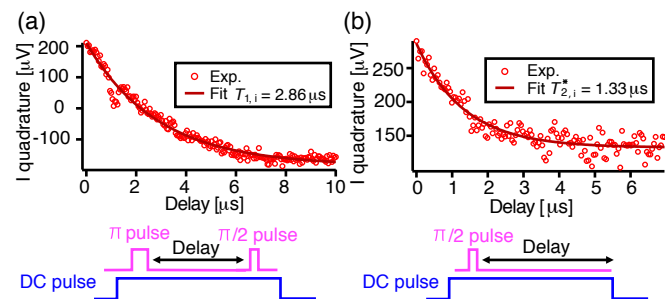


FIG. 7. Intrinsic qubit coherence properties. The intrinsic relaxation time $T_{1,i}$ (a) and the free induction decay time $T_{2,i}^*$ (b) of the qubit are measured at the decoupling point following the pulse sequence indicated in the figure. (a) In order to measure $T_{1,i}$, a resonant π -pulse is delayed from a $\pi/2$ -pulse that projects the qubit state onto the equatorial plane at the end of the sequence [29]. When the SQUID current pulse ends the qubit spontaneously emits and its coherence properties are translated into the field quadrature amplitudes I/Q . (b) The sequence to measure $T_{2,i}^*$ only requires a $\pi/2$ -pulse that excites the qubit in a superposition state at the decoupling point followed by a time delay from the end of the SQUID current pulse which enables the qubit emission. The fact that $T_{2,i}^* < 2T_{1,i}$ indicates the presence of a significant amount of intrinsic pure dephasing $\Gamma_{\phi,i} = (1/2.49) \mu\text{s}^{-1}$.

As explained in Sec. VI, a figure of merit of an on-demand photon generator is the ratio of the intrinsic-to-jitter times. For this particular device, the shortest ob-

served jitter time $T_{1,\text{jit}} = 46$ ns was obtained in Sec. VI. Using the measured intrinsic time $T_{1,i} = 2.86$ μ s from Fig. 7(a), we obtain a ratio $T_{1,i}/T_{1,\text{jit}} \approx 62$.

In order to quantify the efficiency of our circuit as a single-photon source, since the qubit is coupled to an open system, we define the efficiency of the process as the fidelity \mathcal{F} calculated from two density matrices, the target one ρ and the generated one σ , $\mathcal{F} = \text{Tr} [(\sqrt{\rho}\sigma\sqrt{\rho})^{1/2}]$. For that purpose we performed a numerical simulation of the Lindblad master equation of a single driven qubit using QuTip [31]. Taking as a reference the triggered emission 100 ns after the excitation pulse (second trace in Fig. 6) the fidelity \mathcal{F} of a single-photon state is calculated to be above 98%. The fidelity to generate an equal superposition state $|\psi\rangle = (|0\rangle + |1\rangle)/\sqrt{2}$, 100 ns after the excitation pulse corresponds to $\mathcal{F} = 96\%$. Even after 1 μ s, corresponding to the uppermost trace in Fig. 6, these fidelities are still $\mathcal{F} = 84\%$ and $\mathcal{F} = 77\%$, respectively. As it has already been shown possible [32], the planar transmon circuit design can be re-engineered to enhance the values of the intrinsic coherence times in the 10s of microseconds range. In addition, the qubit-line interaction strength can also be increased using novel techniques from recent transmon-resonator experiments [33].

VIII. CONCLUSIONS

We have demonstrated on-demand generation of single photons using a superconducting transmon qubit capacitively coupled to a transmission line. We showed that

the qubit-line interaction can be tuned by controlling the magnetic flux threading a DC-SQUID which acts as an inductive shunt at the end of the transmission line. The coupling can be tuned in real time, allowing the production of arbitrarily shaped single microwave photons with high fidelity. Our decoupling scheme can be directly implemented with other types of superconducting qubits such as flux and fluxonium qubits and also other solid-state qubits such as quantum dots [34]. The technique developed in this work can be generalized to circuits with multiple qubits for the on-demand generation of many-body quantum states of radiation, including superradiant states. Instead of qubits, the decoupling scheme can be equally applied to resonators, potentially enabling the implementation of recent robust quantum communication protocols for microwave thermal fields [3], complementing existing methods of controlled photon emission [35].

IX. ACKNOWLEDGEMENTS

We acknowledge B. L. T. Plourde for providing access to the evaporator at the University of Syracuse for fabrication of the aluminum Josephson circuits and J. J. Nelson and M. Hutchings for their assistance. We also acknowledge fruitful discussion with S. R. Sathyamoorthy and J. Combes. We acknowledge NSERC of Canada, Industry Canada, and the Ontario Ministry of Research and Innovation for funding.

-
- [1] H. J. Kimble, *Nature* **453**, 1023 (2008).
 - [2] B. Hensen *et al.*, *Nature* **526**, 682-686 (2015).
 - [3] B. Vermersch *et al.*, *Phys. Rev. Lett.* **118**, 133601 (2017); Z.-L. Xiang *et al.*, *Phys. Rev. X* **7**, 011035 (2017).
 - [4] J. I. Cirac *et al.*, *Phys. Rev. Lett.* **78**, 3221 (1997).
 - [5] N. Ofek *et al.*, *Nature* **536**, 441 (2016).
 - [6] A. A. Houck *et al.*, *Nature* **449**, 328 (2007).
 - [7] D. Bozyigit *et al.*, *Nature Phys.* **7**, 154 (2011).
 - [8] C. Eichler *et al.*, *Phys. Rev. Lett.* **106**, 220503 (2011).
 - [9] W. F. Kindel, M. D. Schroer, K. W. Lehnert, *Phys. Rev. A* **93** 033817 (2016).
 - [10] M. Pechal *et al.*, *Phys. Rev. X* **4**, 041010 (2014).
 - [11] Y. Yin *et al.*, *Phys. Rev. Lett.* **110**, 107001 (2013).
 - [12] J. Wenner *et al.*, *Phys. Rev. Lett.* **112**, 210501 (2014).
 - [13] C. K. Hong, Y. Ou, L. Mandel *Phys. Rev. Lett.* **59**, 2044 (1987).
 - [14] C. Lang *et al.*, *Nature Phys.* **9**, 345 (2013).
 - [15] D. Roy, C. M. Wilson, O. Firstenberg, *Rev. Mod. Phys.* **89**, 021001 (2017).
 - [16] O. Astafiev *et al.*, *Science* **327**, 840 (2010).
 - [17] I.-C. Hoi *et al.*, *Phys. Rev. Lett.* **107**, 073601 (2011).
 - [18] I.-C. Hoi *et al.*, *Phys. Rev. Lett.* **108**, 263601 (2012).
 - [19] I.-C. Hoi *et al.*, *Phys. Rev. Lett.* **111**, 053601 (2013).
 - [20] A. F. van Loo *et al.*, *Science* **342**, 1494 (2013).
 - [21] Z. H. Peng *et al.*, *Nature Communications* **7**, 12588 (2016).
 - [22] S. Gasparinetti *et al.*, arXiv:1705.05272 (2017).
 - [23] S. R. Sathyamoorthy *et al.*, *Phys. Rev. A* **93** 063823 (2016).
 - [24] K. Koshino, Y. Nakamura, *New Journal of Phys.* **14**, 043006 (2012).
 - [25] I. C. Hoi *et al.*, *Nature Phys.* **11**, 1045 (2015).
 - [26] W. E. Lamb, Jr. and R. C. Retherford, *Phys. Rev.* **72**, 241 (1947).
 - [27] J. Koch *et al.*, *Phys. Rev. A* **76**, 042319 (2007).
 - [28] P. Forn-Díaz *et al.*, *in preparation*.
 - [29] A. A. Abdumalikov, Jr. *et al.*, *Phys. Rev. Lett.* **107**, 043604 (2011).
 - [30] J. E. Gough *et al.*, *Phys. Rev. A* **86**, 043819 (2012).
 - [31] J. R. Johansson, P. D. Nation, F. Nori, *Comp. Phys. Comm.* **183**, 1760 (2012), *ibid.* *Comp. Phys. Comm.* **184**, 1234 (2013).
 - [32] R. Barends *et al.*, *Phys. Rev. Lett.* **111**, 080502 (2013).
 - [33] S. J. Bosman *et al.*, arXiv:1704.06208.
 - [34] X. Mi, *et al.*, *Science* **355**, 156 (2017). A. Stockklauser, *et al.*, *Phys. Rev. X* **7**, 011030 (2017).
 - [35] W. Pfaff *et al.*, arXiv:1612.05238.